Engineering high-affinity PD-1 variants for optimized immunotherapy and immuno-PET imaging

Roy L. Maute[a,b,c,d,1], Sydney R. Gordon[a,b,c,d,1], Aaron T. Mayer[e,f], Melissa N. McCracken[a,b,c,d], Arutselvan Natarajan[e], Nan Guo Ring[a,b,c,d], Richard Kimura[e], Jonathan M. Tsai[a,b,c,d], Aashish Manglik[g], Andrew C. Kruse[h], Sanjiv S. Gambhir[e,f], Irving L. Weissman[a,b,c,d,2], and Aaron M. Ring[a,b,c,d,2]

[a]Institute for Stem Cell Biology and Regenerative Medicine, Stanford University School of Medicine, Stanford, CA 94305; [b]Ludwig Center for Cancer Stem Cell Research and Medicine, Stanford University School of Medicine, Stanford, CA 94305; [c]Stanford Cancer Institute, Stanford University School of Medicine, Stanford, CA 94305; [d]Department of Pathology, Stanford University Medical Center, Stanford, CA 94305; [e]Department of Radiology, Molecular Imaging Program at Stanford (MIPS), James H. Clark Center, Stanford, CA 94305; [f]Department of Bioengineering, Materials Science and Engineering, Stanford University, Stanford, CA 94305; [g]Department of Molecular and Cellular Physiology, Stanford University Medical Center, Stanford, CA 94305; and [h]Department of Biological Chemistry and Molecular Pharmacology, Harvard Medical School, Boston, MA 02115

Contributed by Irving L. Weissman, October 2, 2015 (sent for review April 29, 2015)

Signaling through the immune checkpoint programmed cell death protein-1 (PD-1) enables tumor progression by dampening antitumor immune responses. Therapeutic blockade of the signaling axis between PD-1 and its ligand programmed cell death ligand-1 (PD-L1) with monoclonal antibodies has shown remarkable clinical success in the treatment of cancer. However, antibodies have inherent limitations that can curtail their efficacy in this setting, including poor tissue/tumor penetrance and detrimental Fc-effector functions that deplete immune cells. To determine if PD-1:PD-L1–directed immunotherapy could be improved with smaller, nonantibody therapeutics, we used directed evolution by yeast-surface display to engineer the PD-1 ectodomain as a high-affinity (110 pM) competitive antagonist of PD-L1. In contrast to anti–PD-L1 monoclonal antibodies, high-affinity PD-1 demonstrated superior tumor penetration without inducing depletion of peripheral effector T cells. Consistent with these advantages, in syngeneic CT26 tumor models, high-affinity PD-1 was effective in treating both small (50 mm^3) and large tumors (150 mm^3), whereas the activity of anti–PD-L1 antibodies was completely abrogated against large tumors. Furthermore, we found that high-affinity PD-1 could be radiolabeled and applied as a PET imaging tracer to efficiently distinguish between PD-L1–positive and PD-L1–negative tumors in living mice, providing an alternative to invasive biopsy and histological analysis. These results thus highlight the favorable pharmacology of small, nonantibody therapeutics for enhanced cancer immunotherapy and immune diagnostics.

protein engineering | cancer immunotherapy | PET imaging | PD-1 | PD-L1

Lymphocyte activity is regulated by a complex series of stimulatory, costimulatory, and inhibitory cues. Although the central regulator of T-lymphocyte function is the T-cell receptor (TCR), the balance between positive and negative signaling inputs deeply shapes the response that lymphocytes mount upon exposure to reactive peptide/MHC complexes (1). As a cause and consequence of their development, cancer cells accumulate somatic mutations that distinguish them from noncancerous cells. These tumor "neo-antigens" can be recognized by the TCRs of cytotoxic T lymphocytes and in many cases prompt an endogenous antitumor response by the immune system (2). Thus, immunogenic tumors must exploit, or at least indirectly benefit from, immunosuppressive pathways to escape immune destruction (3).

Expression of the inhibitory programmed cell death ligand-1 (PD-L1) in the tumor environment is a key exemplar of this phenomenon. PD-L1 normally serves to prevent autoimmunity by engaging its receptor, programmed cell death protein-1 (PD-1), on activated T cells (4). Upon binding to either of its two ligands, PD-L1 and PD-L2, PD-1 initiates an inhibitory signaling cascade through its intracellular signaling domains, including an immunoreceptor tyrosine-based inhibitory motif and immunoreceptor tyrosine-based switch motif (5). The result is activation of SHP phosphatases that oppose TCR signaling. Although beneficial in preventing excessive or harmful inflammation under normal conditions, in the context of cancer, tumor and stromal PD-L1 expression presents a barrier to immune function by contributing to the exhaustion of the antitumor lymphocytes that might otherwise clear the malignancy (6). Consequently, the PD-1:PD-L1 pathway has emerged as a critical target for cancer immunotherapy, and monoclonal antibodies that block either side of this inhibitory interaction have demonstrated impressive activity across a broad set of cancer subtypes, even at advanced and metastatic stages of disease (7–11).

Despite their proven utility, antibodies have specific drawbacks as therapeutics, which may be especially pertinent when targeting the PD-1:PD-L1 signaling pathway. For example, PD-1–expressing effector T cells are found infiltrated within solid tissue of PD-L1–expressing tumors (6). This is problematic for antibodies, which are impeded from entering tumors due to their large size (12). It follows that antibodies may therefore fail to completely antagonize PD-1:PD-L1 signaling at the intended therapeutic site within tumors, leading to suboptimal efficacy. An additional limitation of antibodies is their ability to activate cytotoxic immune responses

Significance

Programmed cell death protein-1 (PD-1) and programmed cell death ligand-1 (PD-L1) are key targets in the treatment of cancer, but current antibody-based drugs against this pathway have inherent drawbacks that may limit their effectiveness. We used directed evolution with yeast display to engineer a nonantibody biologic based on the ectodomain of PD-1. High-affinity PD-1 was more effective than anti–PD-L1 antibodies in the treatment of mouse tumor models and could additionally be used as a PET imaging tracer to noninvasively assess the PD-L1 expression status of tumors. This engineered protein thus represents an agent useful for clinical translation and highlights the paradigm of small protein biologics for future drug development.

Author contributions: R.L.M., S.R.G., M.N.M., A.M., A.C.K., S.S.G., I.L.W., and A.M.R. designed research; R.L.M., S.R.G., A.T.M., M.N.M., A.N., N.G.R., R.K., J.M.T., A.M., A.C.K., and A.M.R. performed research; R.L.M., S.R.G., A.M., A.C.K., and A.M.R. contributed new reagents/analytic tools; R.L.M., S.R.G., A.T.M., M.N.M., A.N., N.G.R., J.M.T., A.M., A.C.K., S.S.G., I.L.W., and A.M.R. analyzed data; and R.L.M., S.R.G., N.G.R., A.C.K., I.L.W., and A.M.R. wrote the paper.

Conflict of interest statement: A.M.R., R.L.M., A.C.K., A.M., S.R.G., M.N.M., and I.L.W. are inventors of patents related to the high-affinity PD-1 proteins described in this manuscript. S.R.G. provides paid consulting services for Ab Initio Biotherapeutics, Inc., which licensed the aforementioned patents. A.M.R., R.L.M., A.C.K., and A.M. are founders of Ab Initio Biotherapeutics, Inc.

[1]R.L.M. and S.R.G. contributed equally to this work.

[2]To whom correspondence may be addressed. Email: aaron.ring@yale.edu or irv@stanford.edu.

This article contains supporting information online at www.pnas.org/lookup/suppl/doi:10.1073/pnas.1519623112/-/DCSupplemental.

through natural killer cells and macrophages (e.g., ADCC/ADCP) (13). Although this Fc-mediated effect is in fact required for the efficacy of some immunotherapeutic antibodies (14), it may in part be counterproductive in the case of this receptor–ligand pair. Both PD-1 and PD-L1 are expressed on the surface of antitumor cytotoxic T cells (15, 16), and as such, antibodies targeting PD-1 and PD-L1 may paradoxically result in the undesirable depletion of the very lymphocytes they are intended to activate. Consistent with this hypothesis, treatment with anti–PD-1 antibodies of anti–PD-1 antibodies has been reported to correlate with lower circulating T-cell numbers in patients (17).

To date, most studies of PD-1 or PD-L1 blockade have used monoclonal antibodies. In principle, a soluble fragment of the PD-1 ectodomain could be administered as a competitive antagonist of PD-L1. At 14 kDa in size, this agent would be approximately an order of magnitude smaller than a monoclonal antibody (150 kDa) and also lack an antibody Fc moiety. We thus sought to determine whether such an alternative agent could exhibit improved antitumor responses by avoiding antibody-intrinsic limitations.

Results

Directed Evolution of High-Affinity PD-1 Variants That Antagonize PD-L1. Given its modest affinity for PD-L1 (K_D of 8.2 μM) (18), the wild-type PD-1 ectodomain is a poor candidate to competitively antagonize the PD-1:PD-L1 interaction in a therapeutic context. We thus sought to enhance the affinity of PD-1 for PD-L1 using directed evolution with yeast-surface display. Our engineering strategy used a two-library approach. A first library was used to identify mutational "hotspots" that impart large gains in affinity, and a second library served to determine the optimal combination of beneficial mutations derived from the first library.

To design the initial, "first-generation" library, we studied the crystal structure of the complex between murine PD-1 (mPD-1) and human PD-L1 (hPD-L1) (19) and identified 22 corresponding residues in human PD-1 (hPD-1) at the contact interface with PD-L1 for randomization (Fig. 1*A* and *SI Appendix*, Fig. S1). We displayed this library on the surface of yeast and performed four rounds of selection using recombinant, biotinylated hPD-L1 ectodomain as the selection reagent (Fig. 1*B*, Generation 1). Biophysical characterization of the resulting clones showed a 400–500-fold increase in affinity for hPD-L1, as measured by surface plasmon resonance (Fig. 1*C*). However, the clones exhibited poor biochemical behavior, with decreased expression yield and a tendency toward aggregation. Inspection of the variants (Fig. 1*C*) revealed an average of 16 mutations per clone, with several of the randomized positions converging on a small set of mutations (e.g., V39, N41). Other positions appeared to either diverge (e.g., S48, D52) or have a strict preference for the original wild-type residue

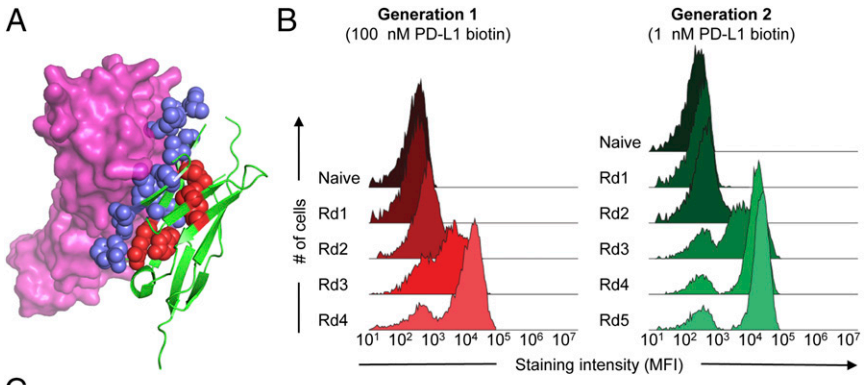

Residue #	39	40	41	43	44	45	48	49	50	51	52	53	56	60	63	65	66	72	82	83	90	96	97	100	102	103	104	105	106	107	111	PD-L1 affinity
hPD-1	V	L	N	Y	R	M	S	N	Q	T	D	K	A	D	Q	G	Q	V	H	M	R	Y	L	A	S	L	A	P	K	A	E	3.88 μM
G1 4-12	H					Q	D	C	K	V	F				T	N	P						Y		T	I	S		G	P		
G1 4-2	H		I	F		Q	L	G		L	F				I	R							V			Y	S		E	I		
G1 4-5	H		V	F		Q	N	G		V	R				E	I	P						V			Y		A	I	V		
G1 4-1	R		V	H		E	G	Y	E			T	S		T	L	P						V		A	F	H		V	I		7.78 nM
G1 4-4	R		V	H		E	N		H	A	Y	T	L		L	F	P						I		T	F	D		R	I		10.7 nM
G1 4-10	H		V	H		L	V	Y			V	L			P	V										Y	D		T	I		
G2 4-12	H	V	V	H	Y	E		G				T								L			V	I						I		218 pM
G2 4-1	H	V	V	H		E		G				T					P			L			V							I		267 pM
G2 4-5	H	V	V	H		E		S				T					P		Q	L			V	V						I		196 pM
G2 4-10	H	V	V	H	Y	D		G				T					P	I		F			I	V						I		
G2 4-14	H	V	V	H	Y	E		G				T					P			F			I	V						I		
G2 4-4	H	I	I	H		E		C				T						I		F		F	V	V						I		
G2 4-22	H	I	I	H		E		G				T						I		F		F	V	V						I		
G2 4-6	R		V	H		E		G				T						I		F		F	V			F				I		
G2 4-7	H	V	V	H		E		G				T						I		L		F	V	V						I		
G2 4-18	H	V	I	H		E		G				T					P	I			K		V	I						I		
G2 4-2	H	I	I	H		E		G				T								L			V	V						I		222 pM
G2 4-23	H	I	I	H		E		G				T					P						V	V						I		
G2 4-3	H	V	I	H	L	E		G				T											V	V						I		101 pM
Consensus 1 (HAC-I)	H	V	I	H		E		G				T											V	V						I		107 pM
Consensus 2 (HAC-V)	H	V	V	H		E		G				T											V	V						I		110 pM

Fig. 1. Directed evolution of high-affinity PD-1 with yeast surface display. (*A*) Model of hPD-1 (green) complexed with hPD-L1 (magenta) constructed by structural alignment of the mPD-1:hPD-L1 complex (PDB ID code 3BIK) with hPD-1 (PDB ID code 3RRQ). Randomized residues of PD-1 are depicted as blue spheres for PD-L1 contact residues and red spheres for core residues. (*B*) Histogram overlays assessing yeast hPD-L1 staining at each round of selection. For the first-generation selections (*Left*), all rounds were stained with 100 nM biotinylated hPD-L1. For the second-generation selections (*Right*), yeast were stained with 1 nM biotinylated hPD-L1. (*C*) Summary of sequences and hPD-L1 affinities for selected PD-1 variants. The position of each mutated position and the corresponding residue in wild-type PD-1 is indicated at the top of the table. Numbering reflects the amino acid position within the mature PD-1 protein after signal peptide cleavage. Italic font indicates mutations that occurred at nonrandomized sites. Blue column shading indicates PD-L1 contact positions that converged in the HAC consensus sequence, whereas red column shading indicates converging core positions. Gray shading denotes those sequences whose hPD-L1 affinities were determined by surface plasmon resonance (SPR).

(e.g., P105, E111). These results suggested that the first-generation variants likely contained a mixture of beneficial mutations, nonfunctional passenger mutations, and deleterious mutations, as would be expected given the very large theoretical diversity of the library ($\sim 10^{20}$) that was sampled with 10^8 yeast transformants.

We thus created a "second-generation" library to eliminate unnecessary and deleterious substitutions, while simultaneously optimizing combinations of mutations that impart enhanced affinity (*SI Appendix*, Fig. S2). As such, we focused the library onto those positions that appeared to be converging away from wild type and also introduced variation at "core" positions within the PD-1 ectodomain (Fig. 1*A*). Through five rounds of selection, we obtained variants that strongly bound PD-L1 (Fig. 1*B*, Generation 2). Compared with wild-type hPD-1, the selected variants bound hPD-L1 with 15,000–40,000-fold enhanced affinity, while showing a strong trend toward convergence onto a consensus sequence of 10 amino acid substitutions comprising eight contact residues and two core residues (Fig. 1*C*). We produced two versions of this high-affinity consensus (HAC) PD-1 that differed only by an isoleucine or valine at position 41 (termed HAC-I and HAC-V, respectively), and we found them to be indistinguishable by affinity or biochemical behavior. Both HAC–PD-1 variants could be easily expressed, were monomeric, and bound hPD-L1 with K_D values of ~100 pM (Fig. 1*C*). This increase in affinity was largely driven by a dramatic reduction in off-rate, yielding dissociation half-lives of ~40 min, compared with less than 1 s for the wild-type hPD-1:hPD-L1 interaction (Fig. 2*A*).

To assess the ability of the engineered PD-1 variants to antagonize PD-L1 on cancer cells, we performed competitive binding experiments on human and murine melanoma cell lines. On human SK-MEL-28 cells, HAC–PD-1 blocked the binding of wild-type PD-1 tetramers with an IC_{50} of 210 pM, a 40,000-fold enhancement in potency compared with blockade with wild-type monomeric hPD-1 (IC_{50}, 8.2 μM) (Fig. 2 *B*, *Left*). Although we performed our selections using hPD-L1, HAC–PD-1 fortuitously also showed enhanced blockade of PD-L1 on murine B16-F10 cells (IC_{50}, 69 nM) in contrast to wild-type hPD-1 (IC_{50}, 2.6 μM), albeit with a decreased potency relative to its blocking on human cells (Fig. 2 *B*, *Center*). To generate a HAC–PD-1 variant that could more efficiently antagonize mPD-L1 for in vivo studies, we fused the sequence of HAC–PD-1 to the dimeric CH3 domain of human IgG1 to create a HAC "microbody" (HACmb; *SI Appendix*, Fig. S3). By virtue of the increased avidity imparted by its dimeric structure, HACmb potently blocked both hPD-L1 (IC_{50}, 55 pM) and mPD-L1 (IC_{50}, 1.2 nM) on SKMEL28 and B16-F10 cells, respectively (Fig. 2 *B*, *Center*). We also sought to characterize the cross-reactivity of HAC–PD-1 for the second ligand of PD-1, PD-L2. In competitive binding experiments on yeast displaying the ectodomain of hPD-L2, we found that HAC–PD-1 did not measurably inhibit the PD-1:PD-L2 interaction, compared with wild-type PD-1 (IC_{50}, 2.5 μM; Fig. 2 *B*, *Right*) Taken in aggregate, these results indicated that the HAC–PD-1 variants could potently and specifically antagonize the PD-1:PD-L1 interaction.

Tumor Penetration and T-Cell Depletion Studies. To assess PD-L1 binding and tumor penetrance of HAC–PD-1 in vivo, we used genome editing techniques to generate sublines of the mouse colon cancer line CT26 that were either definitively negative for mPD-L1 expression or negative for mPD-L1 but constitutively positive for hPD-L1 expression. These sublines could be readily distinguished by in vitro staining with either fluorescently labeled anti–hPD-L1 antibody (clone 29E.2A3) or fluorescently labeled HAC–PD-1 protein (*SI Appendix*, Fig. S4*A*). Using these engineered lines, we engrafted mice bilaterally with PD-L1–negative and hPD-L1–positive tumors. Once the tumors had grown to ~1 cm in diameter, we delivered a mixture of fluorophore-labeled anti–hPD-L1 antibody and fluorophore-labeled HAC–PD-1 by i.p. injection. After 4 h, we dissected the paired tumors and assessed the degree of binding by each agent using both fluorescence microscopy and flow cytometry analysis.

In all PD-L1–negative tumors, histological analysis revealed no detectable binding by either anti–PD-L1 antibody or HAC–PD-1, confirming the specificity of both agents (Fig. 3 *A*, *Bottom*). In contrast, we could clearly observe binding of both the antibody and HAC–PD-1 in hPD-L1–positive tumors, but with strikingly different distributions. Whereas the antibody-associated fluorescence signal was limited to peripheral and perivascular regions of the tumor (Fig. 3 *A*, *Far Left* panel and *SI Appendix*, Fig. S5), HAC–PD-1 staining was widespread (Fig. 3 *A*, *Middle Left* panel and *SI Appendix*, Fig. S5). These observations were supported by FACS analysis of paired hPD-L1–positive and –negative tumors following nonenzymatic dissociation. Neither the antibody nor HAC–PD-1 interacted appreciably with the cells of PD-L1–negative tumors (Fig. 3 *B*, *Left*). However, in hPD-L1–expressing tumors, a clear population was positive for both anti–PD-L1 antibody and HAC–PD-1 binding (Fig. 3 *B*, *Right*), but few if any cells were positive for anti–PD-L1 antibody staining only (Fig. 3 *B*, *Right*). In contrast, many cells were positive for HAC–PD-1 staining alone (Fig. 3 *B*, *Right*). Quantification of this signal over multiple experiments revealed a significant advantage for HAC–PD-1 binding ($P < 1 \times 10^{-4}$), with more than twice as many cells on average bound by HAC–PD-1 than by anti–PD-L1 antibody

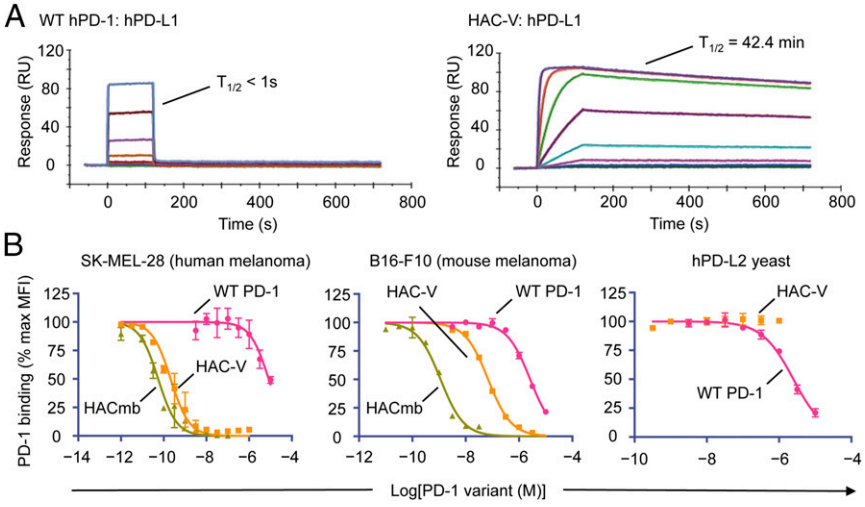

Fig. 2. HAC–PD-1 binds and antagonizes human and mPD-L1 but not PD-L2. (*A*) Representative surface plasmon resonance (SPR) sensorgrams of wild-type PD-1 (*Left*) and HAC-V PD-1 (*Right*) binding to immobilized hPD-L1. (*B*) Competition binding assays of wild-type hPD-1, HAC-V PD-1, or HACmb on human SK-MEL-28 cells (*Left*), mouse B16-F10 cells, or yeast displaying hPD-L2. A total of 100 nM hPD-1/SA AlexaFluor 647 tetramer was used as the probe ligand. Error bars represent s.e.m.

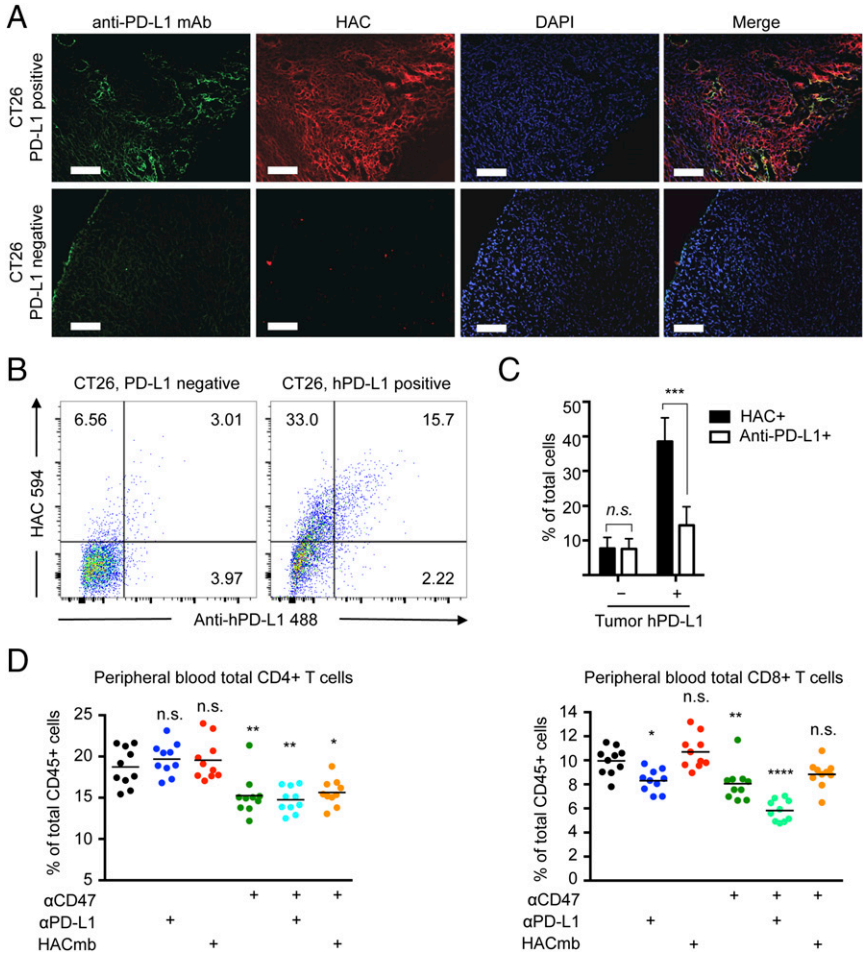

Fig. 3. HAC–PD-1 shows enhanced tumor penetration and does not deplete peripheral T cells. (*A*) Representative fluorescence microscopy images of sectioned CT26 tumors deficient in PD-L1 (*Bottom* row) or transgenic for hPD-L1 (*Top* row) 4 h post-i.p. injection of anti–hPD-L1 AlexaFluor488 (green) and HAC AlexaFluor 594 (red). Nuclei (blue) were labeled with DAPI. (Scale bar, 500 μm.) (*B*) Representative flow cytometry of dissociated tumors from *A* showing HAC AlexaFluor 594 staining versus anti–hPD-L1 AlexaFluor 488 staining. Percentages are given in each positive quadrant. (*C*) Summary of flow cytometry studies from four PD-L1–deficient tumors and four hPD-L1 transgenic tumors. n.s., not significant. ***$P < 0.0001$, two-way ANOVA. Error bars represent s.e.m. (*D*) Relative abundance of peripheral CD4+ T cells (*Left*) or peripheral CD8+ T cells (*Right*) after 3 d of administration of vehicle (PBS), anti-mouse PD-L1, HACmb, anti-mouse CD47, or combinations of these agents to mice engrafted with CT26 tumors. Significance is indicated relative to the PBS control. ns, not significant. *$P < 0.05$, ***$P < 0.001$, one-way ANOVA.

(Fig. 3*C*). This difference was not due to exclusion of anti–PD-L1 antibody binding by high-affinity HAC, as dissociated cells stained in vitro with titrations of the two agents were uniformly double-positive even at a molar excess of HAC:antibody of >100:1 (*SI Appendix*, Fig. S4*B*). Taken together, these data illustrate that HAC–PD-1 was able to bind PD-L1 on tumor cells that were otherwise inaccessible to antibody binding.

In addition to its smaller size, HAC–PD-1 lacks an Fc domain, and therefore we reasoned that, in contrast to antibodies, it would not contribute to an immune-mediated depletion of circulating T-cell numbers. To test this hypothesis, we engrafted wild-type BALB/c mice with tumors derived from the syngeneic colon cancer line CT26, and beginning 14 d postengraftment, we administered daily treatments of PBS, anti-mouse PD-L1 antibody (clone 10F.9G2), or HACmb (used in this case rather than monomer for its enhanced binding to mouse PD-L1). At 72 h after initiation of treatment, mice injected with anti–PD-L1 antibody exhibited a 15% decrease ($P = 0.011$) in circulating peripheral blood CD8+ T cells (Fig. 3*D*). Although PD-L1 expression was detectable on the vast majority of CD4+ and CD8+ cells in tumor-engrafted mice (*SI Appendix*, Fig. S6), the depletive effect was specific to CD8+ T cells, largely sparing the CD4+ compartment (Fig. 3*D*). In contrast to the antibody, daily treatment with HACmb protein had no detectable effect on circulating T-cell levels (Fig. 3*D*).

Although the depletion of CD8+ cells mediated by anti–PD-L1 antibodies was relatively modest, future immunotherapy regimens may involve cotreatment with drugs that activate or disinhibit the innate immune system, such as antibodies that agonize CD137 or inhibit CD47. These agents may thus exacerbate the T-cell–depletive effect of anti–PD-1 and anti–PD-L1 antibodies. To assess this possibility, we administered an anti-mouse CD47 antibody to tumor-engrafted mice either alone or in combination with anti-mouse PD-L1 or HACmb. Treatment with anti-CD47 was sufficient to reduce T-cell populations in both the CD4+ and CD8+ compartments (Fig. 3*D*), and combination treatment with anti-CD47 and anti–PD-L1 further exacerbated the depletion of CD8+ T-cell levels, to ∼60% of their normal proportion (Fig. 3*D*). As expected, HACmb did not contribute to a further depletion in anti-CD47–treated mice (Fig. 3*D*), consistent with our observation that HACmb does not stimulate phagocytosis of PD-L1–positive cells by macrophages in vitro (*SI Appendix*, Fig. S7). These observations suggest that directed agents may have pleiotropic effects on T-cell dynamics that may

include Fc-mediated depletion as well as stimulation of T-cell trafficking into tumors, as has been hypothesized elsewhere (17).

Therapeutic Efficacy of HAC–PD-1 in Syngeneic Tumor Models. Given that HAC–PD-1 agents effectively antagonize both human and mouse PD-L1, we sought to test whether this blockade could reproduce the antitumor effects of anti–PD-L1 antibodies. As an initial test of the in vivo efficacy of HAC–PD-1, we engrafted wild-type, immunocompetent BALB/c mice with syngeneic CT26 tumors, which have previously been shown to be responsive to anti–PD-L1 antibodies (20). After an initial dose-finding experiment for the anti–mPD-L1 antibody (*SI Appendix*, Fig. S8), we compared its antitumor effectiveness with HACmb. On day 7 postengraftment, when tumors had reached an average size of ∼50 mm^3, we randomized mice to treatment cohorts and began daily injections with PBS, antimouse PD-L1 antibody (clone 10F.9G2), or HACmb (Fig. 4*A*). As expected, the tumors of PBS-treated mice grew rapidly. However, by day 14, treatment with either anti–PD-L1 or HACmb had significantly slowed tumor growth relative to controls (Fig. 4*A*; $P = 2 \times 10^{-4}$ and $P < 1 \times 10^{-4}$, respectively), and their efficacy was indistinguishable in this small tumor model (Fig. 4*A*; $P = 0.99$). To assess the mechanism of antitumor activity for HACmb, we also engrafted immunocompromised *Rag2*$^{-/-}$*IL2rg*$^{-/-}$ mice, which lack lymphocytes including T cells, with CT26 tumors. In contrast to wild-type BALB/c mice, HACmb provided no therapeutic benefit in the immunocompromised mice (*SI Appendix*, Fig. S9). Taken together, these results indicated that HACmb activates the adaptive immune system to treat small tumors with an efficacy equal to that of anti–PD-L1.

Many reports of mouse cancer models depend on very early treatment of tumors to demonstrate robust therapeutic effects, as per the design of our initial experiment. However, given the superior tissue penetrance of HAC PD-1, and its ability to block PD-1:PD-L1 interactions without inducing counterproductive depletion of circulating T cells, we hypothesized that its advantages over antibodies might be most apparent when treating

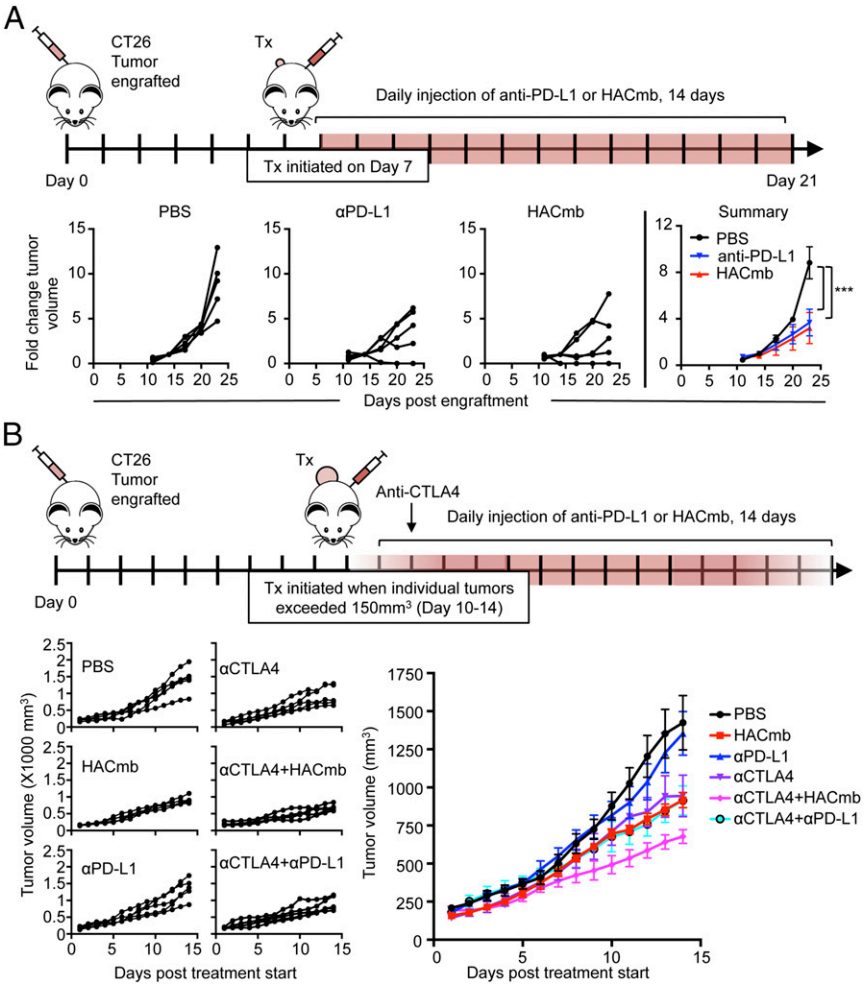

Fig. 4. Antitumor efficacy of HACmb and anti–PD-L1 antibodies in small and large CT26 syngeneic tumor models. (*A*, *Top*) Schematic illustrating the experimental design of the small tumor experiment. Treatment was initiated for all cohorts 7 d after engraftment of tumors. Mice were injected with daily doses of vehicle (PBS), 250 μg anti-mouse PD-L1 (clone 10F.9G2), or 250 μg HACmb for 14 d. (*A*, *Bottom*) Relative growth rates of engrafted tumors, calculated as fold-change from displayed individual tumors (*Left* three panels) or as summary data (*Far Right* panel) over the course of the treatment period. Error bars represent s.e.m. n.s., not significant. ***$P < 0.0001$. (*B*, *Top*) Schematic illustrating the experimental design of the large tumor experiment. Mice were engrafted with CT26 tumors and monitored daily. When an individual tumor exceeded 150 mm^3, the mouse was randomized to a treatment cohort. Tumors were measured daily and received daily treatment with vehicle (PBS), 250 μg anti-mouse PD-L1 (clone 10F.9G2), or 250 μg HACmb for 14 d. Anti-CTLA4 (clone 9D9) was administered as a single dose of 250 μg on day 1 of treatment. (*B*, *Bottom*) Summary data for average tumor growth over the 14-d period of treatment. Error bars represent s.e.m. n.s., not significant. ***$P < 0.001$, two-way ANOVA. Complete statistical analysis at day 14 posttreatment is shown in *SI Appendix*, Table S3.

larger, more challenging tumors. To this end, we initiated an experiment in which we engrafted BALB/c with CT26 cells and monitored their tumor volume daily. Only when an individual tumor achieved a minimum volume of 150 mm^3, or roughly three times the average starting size of our previous experiment, did we randomize the host mouse into a cohort and initiate treatment. This change in experimental protocol had a profound effect on the comparative efficacy of these agents. Whereas anti–PD-L1 antibody and HACmb were equivalent in treating very small CT26 tumors (Fig. 4*A*), in the case of larger tumors, even daily injection of anti–PD-L1 antibody failed to register any measurable efficacy over PBS treatment (Fig. 4*B*; $P = 0.464$). Conversely, HACmb maintained its ability to significantly reduce tumor growth in large tumors over the duration of the study, compared with either PBS-treated (Fig. 4*B*; $P < 1 \times 10^{-4}$) or antibody-treated mice (Fig. 4*B*; $P < 1 \times 10^{-4}$).

Therapeutic combination of immune-stimulating agents, such as anti–PD-1/anti–PD-L1 with anti-CTLA4 antibodies, is emerging as an important paradigm in cancer immunotherapy. We therefore tested whether the superior efficacy of HACmb as a monotherapy would extend to a combination with anti-CTLA4 antibodies. By itself, anti-CTLA4 antibody therapy was effective in this large tumor model, slowing the growth of tumors relative to PBS treatment (Fig. 4*B*; $P < 1 \times 10^{-4}$); however, cotreatment with anti–PD-L1 antibody alongside anti-CTLA4 antibody failed to produce any additional benefit over anti-CTLA4 alone (Fig. 4*B*; $P = 0.756$). In contrast, HACmb improved anti-CTLA4 therapy, as mice treated with a combination of anti-CTLA4 and HACmb had significantly smaller tumors compared with either HACmb (Fig. 4*B*; $P = 0.012$) or anti-CTLA4 alone (Fig. 4*B*; $P = 0.006$).

In summary, these in vivo studies demonstrate that HAC–PD-1 is effective in treating syngeneic mouse tumors. These results illustrate that increases in tumor size disproportionately affect the efficacy of anti–PD-L1 antibodies, potentially rendering them ineffective once tumors surpass a certain size threshold, whereas HAC–PD-1 remains efficacious in a more challenging tumor model. This observation thus suggests that anti–PD-1 or anti–PD-L1 antibodies may not fully capture the maximal therapeutic benefit of PD-1:PD-L1 blockade and that further improvements are possible with optimized therapeutic agents.

In Vivo Detection of PD-L1 Expression by PET with ^{64}Cu-Radiolabeled HAC–PD-1. Expression of PD-L1, by tumor cells or by tumor stroma, has been suggested as a potential biomarker to predict response to PD-1– or PD-L1–directed immunotherapies (21). At present, PD-L1 expression on tumors is most commonly assessed through biopsy followed by immunohistochemical staining. However, in addition to the associated risk and contraindications of the biopsy procedure, the resulting tissue analysis is complicated by the heterogeneous spatial expression pattern of PD-L1 within a tumor. "Immuno-PET" can provide a noninvasive means by which to measure the expression of PD-L1 throughout an entire tumor simultaneously, without the need to excise any tissue. We reasoned that, owing to its high affinity and specificity for PD-L1, as well as its enhanced tissue penetration, a radiolabeled HAC–PD-1 could thus serve as an effective PET probe to assess tumor PD-L1 expression.

To develop a PET tracer based on the HAC–PD-1 scaffold, we conjugated a mutated variant, HAC-N91C, with the thiol-reactive bifunctional chelate DOTA-maleimide (22). Although the apparent hPD-L1 affinity of DOTA–HAC was weaker than its parent sequence HAC-V, DOTA–HAC nonetheless antagonized hPD-L1 1,200-fold more potently than WT PD-1 (*SI Appendix*, Fig. S10*A*). Subsequent radiolabeling with ^{64}Cu produced the hPD-L1–specific radio-protein ^{64}Cu–DOTA–HAC, which possessed a specific activity of 8–10 μCi/μg and radiochemical purity greater than 98%. Furthermore, ^{64}Cu–DOTA–HAC exhibited high immunoreactivity in vitro where it readily bound hPD-L1–positive cells (80.5% ± 1.9%) compared with control hPD-L1–negative cells (8.3% ± 0.1%) (*SI Appendix*, Fig. S10*B*). We used this PET tracer to visualize whole-body hPD-L1 expression in a living mouse.

^{64}Cu–DOTA–HAC showed a strong tumor/muscle and tumor/blood signal (>sixfold enhancement, $P < 0.05$) at 1 h post-injection (Fig. 5*A* and *SI Appendix*, Fig. S12), with high uptake in the kidney, indicating rapid renal clearance of free drug from blood (*SI Appendix*, Figs. S11 *B* and *E* and S12), and high signal in the liver, consistent with copper-specific binding by liver-expressed proteins (Fig. 5*A* and *SI Appendix*, Fig. S12). The lack of signal within PD-L1–negative tumors (Fig. 5*A* and *SI Appendix*, Fig. S11*C*) or in hPD-L1–positive tumors blocked by prior injection of 500 μg of unlabeled HAC–PD-1 (Fig. 5 *A* and *B*) indicated a high degree of specificity of ^{64}Cu–DOTA–HAC–PD-1 for PD-L1 binding. We obtained additional scans at 2, 4, and 24 h (*SI Appendix*, Fig. S11 *A* and *D*) and assessed biodistribution at 1 h and 24 h (*SI Appendix*, Fig. S12). High tumor uptake and favorable tumor-to-background ratios were observed at 1 h after injection, although a strong signal persisted within hPD-L1–positive tumors for at least 24 h (*SI Appendix*, Fig. S11*D*). In sum, the rapid and specific hPD-L1–positive tumor uptake of ^{64}Cu–DOTA–HAC enables its further evaluation for clinical imaging applications.

Discussion

Cancer immunotherapy is a treatment paradigm whose remarkable therapeutic potential is just beginning to be fully realized. Although unprecedented success has been achieved in cancer patients with antibodies targeting the PD-1:PD-L1 axis, nonantibody biologics against this pathway may be able to achieve additional therapeutic gains. In addition to the large size of antibodies, recent work has underscored that their Fc-effector functions can have a substantial and sometimes unexpected impact on the efficacy of cancer immunotherapy agents (23). HAC–PD-1 does not share the antibody-inherent limitations of poor tumor penetration and unwanted depletion of effector T cells. Accordingly, it exerts superior efficacy against a challenging large tumor model compared with anti–PD-L1 antibodies. These results highlight the potential of small-protein biologics as therapeutics for patients and their broad applicability in modulation of the immune system.

In addition to enhanced delivery to tumors, the modular nature of small proteins like HAC–PD-1 enables facile combination with other immunotherapeutics. This is a key consideration in light of the impressive efficacy of combined checkpoint blockade with nivolumab (anti–PD-1) and ipilimumab (anti-CTLA4) in melanoma patients (24) as well as numerous preclinical studies that have demonstrated synergy between antibodies targeting PD-1:PD-L1 and additional immunomodulatory pathways, such as TIM-3 (25), LAG-3 (26), GITR (27), OX-40 (28), and 4-1BB (29). In the case of HAC–PD-1, multispecific agents targeting synergistic immunomodulatory pathways can readily be elaborated by simply fusing multiple small protein modules, including other engineered receptor decoys or single-domain antibodies. This design leverages the coexpression of different immune checkpoint ligands and/or receptors on the same cells to provide enhanced avidity, and thus potency, to the combined agent. Furthermore, multispecific therapeutics could simplify treatment regimens by reducing the number of separately administered drugs and, by extension, reduce the costs associated with their separate manufacture and development.

In considering small proteins as therapeutics, their size presents an important trade-off; although a decreased molecular weight enhances tumor penetration, it also results in increased glomerular filtration and renal losses. Consequently, HAC–PD-1 and other small PD-1:PD-L1 antagonists may need to be administered frequently or continuously to achieve a maximal therapeutic effect. By contrast, the long serum half-life of antibodies in humans makes dosing possible at convenient intervals spaced weeks apart. However, our data indicate that this convenience is counterweighed by the submaximal efficacy of antibodies

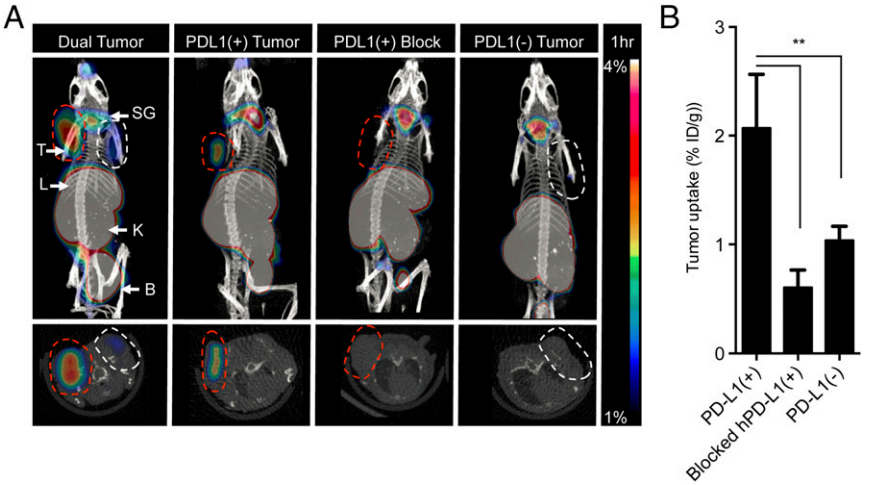

Fig. 5. Micro-PET imaging of hPD-L1 with ^{64}Cu–DOTA–HAC. (*A*) PET-CT images 1 h postinjection of ^{64}Cu–DOTA–HAC (230 μCi/25 μg/200 μL) in NSG mice bearing s.c. hPD-L1(+) (red dashed line) or hPD-L1(–) (white dashed line) CT26 tumors or both hPD-L1(+) and hPD-L1(–) CT26 tumors simultaneously ("dual tumor"). Blocking was performed by injection of 500 μg/200 μL of unlabeled HAC–PD-1 2 h before PET tracer. B, bladder; K, kidneys; L, liver; SG, salivary glands; T, tumor. (*B*) Quantification of tumor uptake in hPD-L1(+) ($n = 4$), hPD-L1(–) ($n = 7$), and blocked CT26 tumors ($n = 3$) 1 h postinjection by ROI analysis, indicated as %ID/g of tissue. There was no PVC correction. Error bars represent SD. *$P < 0.05$, **$P < 0.01$, ***$P < 0.001$, one-way ANOVA.

in the immunotherapeutic setting. Additional study is necessary to determine an optimal balance between classical measures of pharmacokinetics such as drug serum half-life and more direct correlates of therapeutic effectiveness (e.g., target receptor occupancy in tumors).

Although generally well-tolerated compared with other cancer treatments, immunomodulatory drugs such as anti–PD-1 and anti–PD-L1 antibodies have toxicities that range from mild diarrhea to life-threating immune-related adverse events, including autoimmune hepatitis, pneumonitis, and colitis (8, 9). Biomarkers and methods to identify which patients will respond to treatment are urgently needed to avoid unnecessary toxicity in patients who would not otherwise benefit from immunotherapy. Tumor PD-L1 expression by immunohistochemistry (IHC) has thus far proven a partial but imperfect predictor of anti–PD-1/anti–PD-L1 response (30). However, IHC may be an insensitive measure of tumor PD-L1 expression, and it is conceivable that incomplete tumor sampling may mischaracterize PD-L1–positive tumors as negative. Here, we demonstrate the feasibility of using HAC–PD-1 immuno-PET imaging of tumor PD-L1 expression as an alternative to IHC. This noninvasive approach allows simultaneous imaging of the entire tumor and associated metastases, which may differ from the primary tumor in PD-L1 expression status. Furthermore, PET imaging can be used for repeated assessment of the same tumor at different time points (e.g., before and after treatment), thereby yielding a richer set of diagnostic information that would be difficult or impossible to achieve with traditional biopsy/IHC approaches. Future investigation is thus warranted to evaluate the potential of HAC–PD-1 as both a cancer therapeutic and immunodiagnostic.

Methods

Mice. Animal studies were performed in compliance with approval from the Administrative Panel on Laboratory Animal Care at Stanford University. The 6–8-wk-old BALB/c mice, used for syngeneic tumor engraftments and assessment of T-cell levels in response to treatments, were obtained directly from The Jackson Laboratory. Nod.Cg-Prkdc.scid.IL2rg.tm1Wjl/SzJ (NSG) mice, used for in vivo assessment of tumor penetrance and PET studies, were obtained from in-house breeding stocks.

Cell Lines. The human melanoma cell line SK-MEL-28, the murine melanoma cell line B16.F10, and the murine colon carcinoma cell line CT26 were obtained from the ATCC. All cell lines were maintained in a humidified, 5% (vol/vol) CO_2 incubator at 37 °C. SK-MEL-28 cells were subcultured in Eagle's Minimum Essential Medium medium (ATCC) supplemented with 10% (vol/vol) FBS (Thermo Fisher Scientific). B16.F10 cells were subcultured in Dulbecco's Modified Eagle's Medium (Life Technologies) supplemented with 10% FBS and 55 μM 2-mercaptoethanol (Sigma). CT26 cells were grown in RPMI supplemented with 10% (vol/vol) FBS. Genetic variants of CT26 were created by simultaneous transduction of CT26 cells with Cas9-expressing lentivirus and a lentiviral pool encoding a mixture of two mPD-L1-targeting sgRNAs (sequence GGCTCCAAAGGACTTGTACG and GGTCCAGCTCCCGTTCTACA, respectively) designed using the tools at genome-engineering.org (31). At 6 d postinfection, cells were induced to express high levels of PD-L1 through treatment with 100 ng/mL of mouse IFNγ, and at 7 d postinfection, cells were harvested and stained with allophycocyanin (APC)-labeled 10F.9G2 antibody. The negative population was isolated by FACS with a FACS Aria cell sorter, cultured, and subjected to two additional sequential rounds of FACS sorting. This stable negative population was defined as CT26-Δ(mPD-L1). CT26-Δ(mPD-L1) cells were transduced with lentivirus encoding for constitutive, EF1A-driven expression of hPD-L1 to generate a hPD-L1–expressing mouse cancer line. Transduced cells were stained with PE–anti–PD-L1 (clone MIH1, eBioscience) and hPD-L1–expressing cells isolated by FACS to generate the subline CT26-Tg(hPD-L1)-Δ(mPD-L1).

Protein Expression and Purification. The hPD-1 IgV domain (residues 26–147), hPD-L1 IgV and IgC domains (residues 19–239), high-affinity PD-1 variants, and HACmb were assembled as gBlocks (Integrated DNA Technologies) and cloned in-frame into pAcGP67a with a carboxyl-terminal 8× histidine tag for secretion from *Trichoplusia ni* (High Five) cells using baculovirus. The N91C mutation was introduced into HAC-V using PCR-mediated site-directed mutagenesis. Secreted protein was purified from conditioned medium by nickel–nitrilotriacetic acid chromatography and desalted into PBS. Proteins used for functional or in vivo studies in mice were additionally subjected to column washes with Triton X-114 to remove endotoxin. Biotinylated proteins were obtained by addition of a carboxyl-terminal biotin acceptor peptide sequence (GLNDIFEAQKIEWHE) and enzymatic biotinylation with BirA ligase.

Protein Labeling with Amine- and Cysteine-Reactive Probes. HAC-V N91C was expressed and purified as described above and reduced by application of Tris (2-carboxyethyl)phosphine to a final concentration of 1 mM. The reduced protein was combined with a 20-fold molar excess of AlexaFluor 594 C5 maleimide (Life Technologies), AlexaFluor 647 C2 maleimide (Life Technologies), or maleimido–monoamide–DOTA (Macrocyclics) and incubated at room temperature for 1 h and then 4 °C for an additional 12 h. Excess-free probe was removed by desalting the reaction mixture into PBS using a VivaSpin protein concentrator (Sartorius Stedim). For DOTA–HAC, reacted protein was exchanged into Hepes buffered saline (10 mM Hepes pH 7.4, 150 mM NaCl) and concentrated to ∼5 mg/mL. The number of chelators

coupled per antibody (c/a) was estimated with matrix-assisted laser desorption/ionization time-of-flight mass spectrometry by comparison of unreacted HAC–N91C and HAC–DOTA.

Low-endotoxin/azide-free anti–hPD-L1 (clone 29E.2A3, BioLegend) was labeled with an eightfold molar excess of AlexaFluor 488 NHS ester for 2 h at room temperature (Life Technologies). Free dye was quenched by addition of Tris pH 8.0 to a final concentration of 20 mM and the labeled antibody desalted with a VivaSpin protein concentrator.

Yeast Display and Directed Evolution. The IgV domains of hPD-1 (residues 26–147), the IgV and IgC domains of hPD-L1 (residues 19–132), and hPD-L2 (residues 20–123) were displayed on the surface of *Saccharomyces cerevisiae* strain EBY100 as N-terminal fusions to Aga2 using the pYAL vector as previously described (32).

Construction and selection of the first-generation hPD-1 library. Twenty-two potential PD-L1 contact residues in hPD-1 were identified from homologous positions in the structure of mPD-1 complexed to hPD-L1 [Protein Data Bank (PDB ID) code 3SBW]. A library randomizing these residues (*SI Appendix*, Fig. S1) was constructed using assembly PCR with the primers listed in *SI Appendix*, Table S1. The library had a theoretical diversity of $\sim 9.5 \times 10^{19}$ unique protein sequences. The PCR products were further amplified with primers containing homology to the pYAL vector and coelectroporated together with linearized pYAL into EBY100 yeast. The resulting library contained 0.9×10^8 transformants.

Transformed yeast were recovered and expanded in liquid synthetic dextrose medium with casamino acids (SDCAA) medium at 30 °C and induced by dilution 1:10 into liquid synthetic galactose medium with casamino acids (SGCAA) medium and cultured at 20 °C for 24 h. Appropriate numbers of induced yeast were used in each round to ensure at least 10-fold coverage of the expected diversity of the library at each step, and not less than 10^8 cells. All selection steps were carried out at 4 °C using MACS buffer (PBS with 0.5% BSA and 2 mM EDTA). Before each round, preclearing against streptavidin (SA) AlexaFluor 647 (produced in-house) was performed with anti-Cy5/Alexa Fluor 647 microbeads (Miltenyi) and an LD MACS column (Miltenyi). For rounds 1–3, positive selection was performed by labeling-induced yeast with 1 μM biotinylated hPD-L1 for 1 h at 4 °C, followed by secondary staining with SA AlexaFluor 647 and magnetic selection with anti-Cy5/AlexaFluor 647 microbeads and an LS MACS column (Miltenyi). For round 4, positive selection was performed by staining with 10 nM biotinylated hPD-L1 and secondary labeling with SA AlexaFluor 647. Display levels were determined by staining with AlexaFluor 488-conjugated anti-cMyc (Cell Signaling Technologies), and the top 1% of display-normalized hPD-L1 binders were isolated using FACS with a FACS Aria cell sorter. After each round of selection, recovered yeast were expanded in SDCAA medium at 30 °C overnight and later induced at 20 °C by a 1:10 dilution into SGCAA medium for 24 h.

Construction and selection of the second-generation hPD-1 library. The second-generation library was designed to randomize 10 contact positions from the first library that demonstrated convergence away from the wild-type residue as well as seven additional core positions. The design (*SI Appendix*, Fig. S2) had a theoretical diversity of $\sim 9.1 \times 10^9$ unique protein sequences. As for the first-generation library, the second-generation library was constructed by assembly PCR with primers listed in *SI Appendix*, Table S2 and coelectroporated with pYAL into EBY100 yeast. The resulting library yielded 1.2×10^8 transformants.

The second-generation library was selected similarly to the first-generation library with a few modifications. Rounds 1–3 were performed by staining with 1 μM biotinylated hPD-L1 and magnetic bead selection as described above. For rounds 4 and 5, kinetic selection was performed to select for variants with decreased off-rates. Briefly, yeast were stained with 10 nM biotinylated hPD-L1 for 1 h at 4 °C. After washing with MACS buffer, the yeast were then incubated with 1 μM nonbiotinylated hPD-L1 for 6 h at room temperature with agitation. Postcompeted yeast were then stained with SA AlexaFluor 647 and AlexaFluor 488-conjugated anti-cMyc, and the top 1% of display-normalized binders were isolated by FACS sorting.

Surface Plasmon Resonance. Experiments were conducted using a Biacore T100 and carried out at 25 °C. Biotinylated PD-L1 was immobilized onto a Biacore SA sensor chip (GE Healthcare) to yield an *R*max of ~100 RU. An unrelated biotinylated protein (the IgSF domain of human CD47) was immobilized onto the reference surface with a matching RU value to control for nonspecific binding. Measurements were made with serial dilutions of the PD-1 variants in Hepes buffered saline-P+ buffer (10 mM Hepes pH 7.4, 150 mM NaCl, 0.005% surfactant P20) as indicated in Fig. 2*A*. The PD-L1 surface was regenerated by three 60-s injections of 50% vol/vol ethylene glycol and 100 mM glycine pH 9.5. All data were analyzed with the Biacore T100 evaluation software version 2.0 with a 1:1 Langmuir binding model.

PD-1 Cell Competition Binding Assays. WT PD-1 tetramer was formed by incubating biotinylated WT PD-1 with AlexaFluor 647-conjugated SA at a molar ration of 4:1. PD-L1 expression was induced on GFP-luciferase+ SK-MEL-28 cells by overnight simulation with 2,000 U/mL of human IFNγ. We then combined 100 nM WT PD-1 tetramer with titrating concentrations of WT PD-1 monomer, HAC-V, or HACmb and simultaneously added them to 100,000 induced SK-MEL-28 cells. Cells were incubated with the reagent mixtures on ice for 60 min and then washed to remove unbound tetramer. AlexaFluor 647 fluorescence intensity was quantified by flow cytometry using an Accuri C6 flow cytometer (BD Biosciences).

In Vivo Tumor Penetration Studies. The 6–8-wk-old female NSG mice were injected s.c. with 1×10^6 cells of the genetically modified colon cancer line CT26-Δ(mPD-L1) in their left shoulder, and 1×10^6 cells of CT26-Tg(hPD-L1)-Δ(mPD-L1) in their right shoulder, in a 50 μL suspension of 75% (vol/vol) RPMI (Life Technologies) and 25% (vol/vol) medium-density matrigel (Corning) for each injection. After 14 d, when tumors had grown to ~1 cm in diameter, mice were injected intraperitoneally with a mixture of 100 μg AlexaFluor 488-conjugated anti–PD-L1 antibody (clone 29E.2A3, BioLegend) and 100 μg AlexaFluor 594-conjugated HAC–PD-1 monomer. After 4 h, mice were euthanized and their tumors were dissected. After several rounds of washing with cold PBS to remove excess blood, each tumor was cut in half. One half was incubated in a solution of 1% PFA in PBS overnight at 4 °C with rocking, washed in PBS, and embedded in Tissue Tek Optimal Cutting Temperature (Sakura). The 7-μm frozen sections of these tissues were cut and thawed for 30 min, washed in acetone at 4 °C for 4 min, air-dried for 10 min, washed in PBS (three times, 5 min each), and labeled with Hoechst 33342 (Invitrogen) before mounting with Fluoromount G (Southern Biotech). Slides were visualized on an Eclipse e800 fluorescent microscope (Nikon) at 10× or 20× magnification. Basic photo processing, including fluorescence channel false-coloring, channel merge, and brightness and contrast adjustment, were performed using Adobe Photoshop (Adobe). For FACS analysis, the second half of each tumor was finely minced with a straight razor, and the minced tissue was pressed through a 100-μM mesh cell strainer, rinsed with PBS, and finally passed through a 40-μM cell strainer while in liquid suspension. Samples were kept as close to 4 °C as possible throughout all steps of processing. Finally, the resulting single-cell suspension was fixed in a 1% PFA solution and analyzed for antibody- and HAC-derived fluorescence signal on an LSRFortessa FACS Analyzer (BD Biosciences).

T-Cell Depletion Studies. The 6–8-wk-old wild-type female BALB/c mice were shaved on their lower dorsum and injected s.c. with 1×10^6 cells of the colon cancer line CT26 in a 50 μL suspension of 75% (vol/vol) RPMI (Life Technologies) and 25% (vol/vol) medium-density matrigel (Corning). Mice whose tumors failed to engraft within 7 d by visual inspection were excluded from further study. Those with palpable tumors were randomized into treatment groups, 10 mice per group, using the tools at random.org. Mice were treated for 3 d by once-daily i.p. injections of 100 μL PBS, 250 μg of anti–PD-L1 antibody (clone 10F.9G2, BioXcell), or 250 μg purified HACmb protein, each adjusted to a concentration of 2.5 mg/mL. For anti-CD47 studies, mice were injected with 25 μg anti-CD47 (clone MIAP301) as a "priming" dose and, then starting 3 d later, were treated daily with 250 μg anti-CD47, anti-CD47 plus anti–PD-L1, or anti-CD47 plus HACmb. After 3 d of treatment, peripheral blood and lymph nodes were collected from each mouse and stained with the following panel of antibodies (BioLegend): AlexaFluor488 CD45 (clone 30-F11), PerCP-Cy5-5 CD8 (clone 53–6.7), AlexaFluor700 Nk1.1 (clone PK136), APC-Cy7 B220 (clone RA3-6B2), PE-Dazzle CD11b (clone M1/70), PE-Cy5 F4/80 (clone BM8), PE-Cy7 CD4 (GK1.5), and APC PD-L1 (clone 10F.9G2). DAPI was used as a viability stain. Samples were analyzed on an LSRFortessa FACS Analyzer (BD Biosciences).

CT26 Tumor Models. The 6–8-wk-old wild-type female BALB/c mice were shaved on their lower dorsum and injected s.c. with 1×10^6 cells of the colon cancer line CT26 in a 50 μL suspension of 75% (vol/vol) RPMI (Life Technologies) and 25% (vol/vol) medium-density matrigel (Corning). Mice whose tumors failed to engraft within 7 d by visual inspection were excluded from further study. For small tumor treatment studies, mice were randomized into cohorts using the list randomization tools at random.org, and treatments were administered starting 7 d postengraftment for all mice. In these small tumor studies, digital caliper measurements were taken every third day, and values were graphed as fold change, as normalized to the measured values on day 10. For large tumor studies, mice were engrafted as

described above, and starting at day 8, tumors were measured on a daily basis. Mice were individually sorted into treatment cohorts, and treatment was initiated only when tumors reached a threshold of 150 mm^3, ~10–14 d postengraftment in all cases. Digital caliper measurements were taken every day for every mouse in the large tumor experiment for the duration of treatment. To reduce random day-to-day variability in measured values, the graphed tumor volumes in this experiment are averages as evaluated within a sliding window that includes the current day, the previous day, and the next day's measurements. Values from the large tumor study were graphed as absolute tumor volume (mm^3). In both experiments, mice were given daily treatment injections intraperitoneally for 14 d with 100 μL PBS, 250 μg anti–PD-L1 antibody (clone 10F.9G2, BioXcell), or 250 μg purified HACmb protein, each adjusted to a concentration of 2.5 mg/mL. Tumors were approximated as ellipsoids with two radii, x and y, where x is the largest measurable dimension of the tumor and y is the dimension immediately perpendicular to x: Volume = (4/3) * (π) * (x/2) * (y/2) (2).

^{64}Cu Labeling of DOTA–HAC. DOTA–HAC was radiolabeled with $^{64}CuCl_2$ (University of Wisconsin, Madison); 500 μg of DOTA–HAC in 200 μL of 0.1 mM ammonium acetate buffer (pH 5.5) was reacted with ~370 MBq (~10 mCi) of neutralized $^{64}CuCl_2$ solution at 37 °C for 1 h. After incubation, 5 mM EDTA pH 7.0 was added at room temperature for 15 min to scavenge unchelated $^{64}CuCl_2$ in the reaction mixture. Purification of ^{64}Cu–DOTA–HAC was performed using an SEC 3000 HPLC with a flow rate of 1.0 mL/min (0.1 M phosphate buffer, pH 7.0). Radiochemical purity was assessed by radio-HPLC. The final dose of radioconjugate was passed through a 0.2-μm filter into a sterile vial.

Radiotracer Cell Binding Assay. An in vitro cell binding assay was performed using CT26-Tg(hPD-L1)-Δ(mPD-L1) cells, CT26-Tg(hPD-L1)-Δ(mPD-L1) cells preblocked with 1 μM HAC-V, and control CT26-Δ(mPD-L1) cells. We aliquotted 2.5×10^5 cells in 0.1 mL in triplicate and washed them with PBSA (PBS supplemented with 1% BSA). Each tube was incubated with 0.1 mL and 5 nmol/L ^{64}Cu–DOTA–HAC (5–6 MBq/nmol) for 45 min. After incubation, cells were washed thrice with PBSA. Activity in each cell pellet was quantified using a gamma counter (1470 WIZARD Automatic Gamma Counter; Perkin–Elmer).

Small-Animal Micro-PET Imaging. NSG mice bearing s.c. hPDL1-positive ($n = 4$) or hPDL1-negative ($n = 7$) CT26 tumors were injected i.v. with ^{64}Cu–DOTA–HAC (~230 μCi/25 μg protein/200 μL PBS). One group also received a blocking dose ($n = 3$) of 500 μg/200 μL cold HAC 2 h preinjection of PET radiotracer. Mice were anesthetized and imaged on a Siemens Inveon small-animal multimodality PET/CT system (Preclinical Solutions; Siemens Healthcare) at time points of 1, 2, 4, and 24 h postinjection. CT raw images were acquired in the second bed position at 80 kVp/500 μA, half-scan 220° of rotation, 120 projections per bed position, with a 50-μM focal spot size using a cone beam micro–X-ray source, and a 2,048 × 3,072 pixel X-ray detector. Cone-beam filtered back-projection and a Shepp-Logan filter were used to reconstruct CT datasets. Static PET images were acquired with the default coincidence timing window of 3.4 ns and energy window of 350–650 keV on the basis of attenuation correction from the CT scans. PET scan acquisition time lengths of 3 min (1, 2 h), 5 min (4 h), and 10 min (24 h) were chosen based upon time postinjection. PET datasets were reconstructed using the 2D ordered-subset expectation maximization (OSEM 2D) algorithm (33). Image analysis was performed using the Inveon Research Workspace. For each micro-PET scan, 3D regions of interest (ROIs) were drawn over the liver, spleen, kidneys, and tumor on decay-corrected whole-body images. Percent injected dose per gram (%ID/g) of tissue in each organ was obtained from dividing the mean pixel value in the ROI (nCi/cc) by the total injected dose. Partial volume correction was not performed. Statistical analysis was performed by two-way ANOVA (GraphPad).

Biodistribution Studies. After completion of micro-PET/CT imaging at the 1 and 24 h postinjection time point, mice were euthanized and dissected for biodistribution. Blood and organs (heart, lungs, liver, spleen, pancreas, stomach, small intestine, large intestine, kidney, muscle, bone, bone marrow, skin, brain, tumor, and tail) were collected and weighed. The cpm values for each organ from gamma countermeasurements were converted to %ID/g of tissue. Data were decay-corrected to injection time.

ACKNOWLEDGMENTS. The authors thank T. Storm, T. Naik, A. McCarty, A. Cha, D. Tseng, and J. P. Volkmer for technical assistance, discussions, and reagents. The authors thank members of the I.L.W. laboratory and the Stanford Shared FACS Facility for advice and helpful discussions. Research reported in this publication was supported by the D. K. Ludwig Fund for Cancer Research (to I.L.W.); National Cancer Institute (NCI) ICMIC P50A114747, the Canary Foundation, Ben and Catherine Ivy Foundation, and Sir Peter Michael Foundation (S.S.G.); NCI PHS T32CA09151 (to M.N.M.); Stanford Medical Scientist Training Program NIH-GM07365 (to A.M.R., J.M.T., and A.M.); and a Cancer Research Institute Irvington Fellowship (to R.L.M.).

1. Pardoll DM (2012) The blockade of immune checkpoints in cancer immunotherapy. *Nat Rev Cancer* 12(4):252–264.
2. Blankenstein T, Coulie PG, Gilboa E, Jaffee EM (2012) The determinants of tumour immunogenicity. *Nat Rev Cancer* 12(4):307–313.
3. Hanahan D, Weinberg RA (2011) Hallmarks of cancer: The next generation. *Cell* 144(5):646–674.
4. Francisco LM, Sage PT, Sharpe AH (2010) The PD-1 pathway in tolerance and autoimmunity. *Immunol Rev* 236:219–242.
5. Chemnitz JM, Parry RV, Nichols KE, June CH, Riley JL (2004) SHP-1 and SHP-2 associate with immunoreceptor tyrosine-based switch motif of programmed death 1 upon primary human T cell stimulation, but only receptor ligation prevents T cell activation. *J Immunol* 173(2):945–954.
6. Iwai Y, et al. (2002) Involvement of PD-L1 on tumor cells in the escape from host immune system and tumor immunotherapy by PD-L1 blockade. *Proc Natl Acad Sci USA* 99(19):12293–12297.
7. Brahmer JR, et al. (2012) Safety and activity of anti-PD-L1 antibody in patients with advanced cancer. *N Engl J Med* 366(26):2455–2465.
8. Topalian SL, et al. (2012) Safety, activity, and immune correlates of anti-PD-1 antibody in cancer. *N Engl J Med* 366(26):2443–2454.
9. Hamid O, et al. (2013) Safety and tumor responses with lambrolizumab (anti-PD-1) in melanoma. *N Engl J Med* 369(2):134–144.
10. Motzer RJ, et al. (2015) Nivolumab for metastatic renal cell carcinoma: Results of a randomized phase II trial. *J Clin Oncol* 33(13):1430–1437.
11. Rizvi NA, et al. (2015) Activity and safety of nivolumab, an anti-PD-1 immune checkpoint inhibitor, for patients with advanced, refractory squamous non-small-cell lung cancer (CheckMate 063): A phase 2, single-arm trial. *Lancet Oncol* 16(3):257–265.
12. Lee CM, Tannock IF (2010) The distribution of the therapeutic monoclonal antibodies cetuximab and trastuzumab within solid tumors. *BMC Cancer* 10:255.
13. Scott AM, Wolchok JD, Old LJ (2012) Antibody therapy of cancer. *Nat Rev Cancer* 12(4):278–287.
14. Simpson TR, et al. (2013) Fc-dependent depletion of tumor-infiltrating regulatory T cells co-defines the efficacy of anti-CTLA-4 therapy against melanoma. *J Exp Med* 210(9):1695–1710.
15. Gros A, et al. (2014) PD-1 identifies the patient-specific $CD8^+$ tumor-reactive repertoire infiltrating human tumors. *J Clin Invest* 124(5):2246–2259.
16. Talay O, Shen CH, Chen L, Chen J (2009) B7-H1 (PD-L1) on T cells is required for T-cell-mediated conditioning of dendritic cell maturation. *Proc Natl Acad Sci USA* 106(8):2741–2746.
17. Brahmer JR, et al. (2010) Phase I study of single-agent anti-programmed death-1 (MDX-1106) in refractory solid tumors: Safety, clinical activity, pharmacodynamics, and immunologic correlates. *J Clin Oncol* 28(19):3167–3175.
18. Cheng X, et al. (2013) Structure and interactions of the human programmed cell death 1 receptor. *J Biol Chem* 288(17):11771–11785.
19. Lin DY, et al. (2008) The PD-1/PD-L1 complex resembles the antigen-binding Fv domains of antibodies and T cell receptors. *Proc Natl Acad Sci USA* 105(8):3011–3016.
20. Deng L, et al. (2014) Irradiation and anti-PD-L1 treatment synergistically promote antitumor immunity in mice. *J Clin Invest* 124(2):687–695.
21. Herbst RS, et al. (2014) Predictive correlates of response to the anti-PD-L1 antibody MPDL3280A in cancer patients. *Nature* 515(7528):563–567.
22. Miao Z, Ren G, Liu H, Jiang L, Cheng Z (2010) Small-animal PET imaging of human epidermal growth factor receptor positive tumor with a 64Cu labeled affibody protein. *Bioconjug Chem* 21(5):947–954.
23. Dahan R, et al. (2015) FcγRs modulate the anti-tumor activity of antibodies targeting the PD-1/PD-L1 axis. *Cancer Cell* 28(3):285–295.
24. Wolchok JD, et al. (2013) Nivolumab plus ipilimumab in advanced melanoma. *N Engl J Med* 369(2):122–133.
25. Sakuishi K, et al. (2010) Targeting Tim-3 and PD-1 pathways to reverse T cell exhaustion and restore anti-tumor immunity. *J Exp Med* 207(10):2187–2194.
26. Woo SR, et al. (2012) Immune inhibitory molecules LAG-3 and PD-1 synergistically regulate T-cell function to promote tumoral immune escape. *Cancer Res* 72(4):917–927.
27. Lu L, et al. (2014) Combined PD-1 blockade and GITR triggering induce a potent antitumor immunity in murine cancer models and synergizes with chemotherapeutic drugs. *J Transl Med* 12:36.
28. Guo Z, et al. (2014) PD-1 blockade and OX40 triggering synergistically protects against tumor growth in a murine model of ovarian cancer. *PLoS One* 9(2):e89350.
29. Takeda K, et al. (2010) Combination therapy of established tumors by antibodies targeting immune activating and suppressing molecules. *J Immunol* 184(10):5493–5501.
30. Robert C, et al. (2015) Nivolumab in previously untreated melanoma without BRAF mutation. *N Engl J Med* 372(4):320–330.
31. Hsu PD, et al. (2013) DNA targeting specificity of RNA-guided Cas9 nucleases. *Nat Biotechnol* 31(9):827–832.
32. Ring AM, et al. (2013) Adrenaline-activated structure of beta2-adrenoceptor stabilized by an engineered nanobody. *Nature* 502(7472):575–579.
33. Natarajan A, Hackel BJ, Gambhir SS (2013) A novel engineered anti-CD20 tracer enables early time PET imaging in a humanized transgenic mouse model of B-cell non-Hodgkins lymphoma. Clin *Cancer Res* 19(24):6820–6829.